Archives of Civil and Mechanical Engineering (2021) 21:23
https://doi.org/10.1007/s43452-020-00161-8

ORIGINAL ARTICLE

Adiabatic shearing mechanism on Al-4.2%Cu alloy bars subjected to electromagnetic loading

Xu Zhang[1] · Yunkai Huang[1] · Shengfei Meng[2] · Congcong Zhu[3] · Guangyao Li[3] · Junjia Cui[3]

Received: 4 August 2020 / Revised: 24 November 2020 / Accepted: 7 December 2020 / Published online: 27 January 2021
© Wroclaw University of Science and Technology 2021

Abstract

This paper proposed an electromagnetic loading process with the high-speed impact. Al-4.2% Cu alloy bars were used to employ electromagnetic impact (EI) experiments. Deformation mechanism and microstructure evolution of EI samples were revealed by theoretical model and microstructure characterizations. The EI process had impact force (peak value 40 kN) and impact velocity (peak value 6.7 m/s) during a short time period (1.25 ms). Adiabatic shearing mechanism dominated the whole deformation process, causing that significant microstructure characteristic was adiabatic shear bands (ASBs). The theoretical analysis implied that the formation of ASBs was accounted for the radial velocity gradient. Most plastic deformations concentrated in ASBs, and approximately pure shear deformations resulted in adiabatic temperature rise of 0.33–0.42 T_m inside ASBs. The width of ASBs was about 135 μm, in which original equiaxial grains were elongated into laminated sub-structures. TEM observations showed multi-slip systems were simultaneously actuated due to severe shear deformations. High dislocation density and dislocation tangles distributed with the ASBs. Adiabatic temperature rise and distorted energies drove sub-grains rotate into recrystallization grains (70–280 nm) with large angle grain boundaries. The needed maximum time (45 μs) for rotational dynamic recrystallization was far less than that of plastic deformation, indicating that rotational dynamic recrystallization mechanism contributed to the formation of recrystallization grains.

Keywords Electromagnetic loading · Al-4.2%Cu alloys · Adiabatic shearing · Recrystallization

1 Introduction

To achieve energy saving and emission reduction, lightweight materials were more and more widely used in automobile and aerospace manufacturing fields. Aluminum and aluminum alloys were the ideal engineering materials due to low density, high specific strength and good thermal conductivity [1]. Among aluminum alloys, Al–Cu alloys could obtain good mechanical properties by deformation-aging treatments, and were usually manufactured into load-bearing parts. These parts frequently understood impact loads (high strain rates) under its service conditions. Consequently, many studies have presently focused on deformation mechanism and microstructure evolution under high strain rates.

Impact loading processes mainly included Split Hopkinson Bar technology [2], drop hammer [3] and electromagnetic forming [4]. The proposed electromagnetic loading process in this work used pulsed magnetic forces to impact samples. This technology had some characteristics of high loading speed, great peak forces and easily-controlled deformation [5, 6]. An important deformation mechanism under high strain rate loading was adiabatic shearing process. Adiabatic shear bands (ASBs) as significant microstructure characteristic were narrow bands, in which plastic deformations were highly concentrated. Adiabatic shear band was extensively investigated from three aspects: its formation mechanism and microstructure evolution within it. Investigations by Wright [7] showed that adiabatic shear band was a deformation localization phenomenon resulting from thermal softening. Tresca [8] first observed localized heating due to non-uniform distribution of plastic deformations during

✉ Xu Zhang
ddzhangxu@126.com

1 College of Automotive and Mechanical Engineering, Changsha University of Science and Technology, Changsha 410114, China

2 Advanced Institute of Materials Science, Changchun University of Technology, Changchun 130012, China

3 State Key Laboratory of Advanced Design and Manufacturing for Vehicle Body, Hunan University, Changsha 410082, China

the forging experiment. Deformation localization inside ASBs inevitably led to notable temperature rise. Zener and Hollomon [9] proposed an adiabatic shear instability model based on a constitutive model which considered strain hardening, strain rate hardening and thermal softening effects. Adiabatic shear instability occurred when thermal softening exceeded strain hardening and strain rate hardening. Bai [10] also proposed thermo-plastic instability model. The heats transferred from plastic works caused materials softening, which in turn promoted plastic deformations. More heats were generated again due to intensified plastic deformations. The formation of ASBs was accounted for the cyclic mutual promotion between plastic deformation and thermal softening. Thermal softening caused by adiabatic temperature rise was certified by many researchers. Ranc et al. [11] measured temperature rise during the ASB initiation and propagation stages of Ti-6Al-4V materials subjected to torsional loading. Results showed that temperature rise was 100–300 °C for the ASB initiation stage, and the maximum temperature rise reached up to 1100 °C for the ASB propagation stage. Li et al. [12] reported that theoretical temperature rise of ultrafine-grained titanium was 900 K (0.46 T_m) at a shear strain 4.5. In addition, Simulations by Li et al. [13] demonstrated that maximum adiabatic temperature rise could reach 400 K for nanostructured face-centered cubic alloys. Dynamic fracture of materials was rooted from the formation of ASBs [14]. Consequently, some catastrophic engineering failures were avoided by investigating the formation mechanism of ASBs, and this failure mode could also be used to develop new technologies (such as high-speed machine cutting) [15]. Moreover, the ASB as a deformation mechanism could contribute to the formation of difficult-to-deformation materials. It is quite helpful to examine residual microstructures within adiabatic shear bands to reveal possible evolution mechanisms. Therefore, many investigations were conducted on microstructure evolution with the ASBs. Most results [16–18] presented that grains in ASBs were refined into nanometer scale, and these ultrafine grains were generated by dynamic recrystallization mechanism. During conventional recrystallization process, heating temperature and holding time were two vital factors. The recrystallization grains generally underwent a nucleation and growth process. Distinguishing from traditional deformation processes, the localized deformations were completed within very short time. The deformation conditions with high strain rate were converted from isothermal process to adiabatic process. Consequently, dynamic recrystallization mechanisms under high strain rate should be different from that of traditional mechanisms. Hines et al. [19] proposed a model based on a "bicrystal" approach using crystal plasticity theory to predict sub-grain misorientation evolution. It was considered that the recrystallized grains within ASBs were formed by mechanical rotation of sub-grains. Furthermore, rotational dynamic recrystallization mechanism, which was widely approved, was proposed by Meyers et al. [20, 21]. Under the driving of adiabatic temperature rise and distortion energies stored by high dislocation densities, the sub-grain boundaries were rotated by 30°. The small angle grain boundaries were evolved into large angle grain boundaries, resulting in equiaxial recrystallization grains. Based on the established model, it was found that formations of recrystallization grains in ASBs of copper [22], titanium alloys [23, 24] and aluminum alloys [25] accorded with this mechanism. The needed time of sub-grain rotations was far less than deformation time by theoretical calculations. Most studies mentioned above were employed using the Split Hopkinson Bar (SHB) technology. In this work, the proposed electromagnetic impact (EI) loading process could give rise to a high strain rate. The loading characteristic of EI process was different from that of SHB technology.

The aim of this article is to explore the formation mechanism of ASBs and microstructure evolution under electromagnetic loading. ASBs of Al-4.2%Cu alloy bars were prepared by electromagnetic impact (EI) experiments. First, the loading characteristic of the EI process was established though loading tests. Second, the formation mechanism of ASBs was revealed by a theoretical model. Finally, microstructure evolution within ASBs was revealed by scanning electron microscope (SEM) and transmission electron microscope (TEM) characterizations.

2 Materials and methods

2.1 Materials

In this work, the as-received specimens were Al-4.2%Cu alloy bars with the diameter of 6 mm and height of 9 mm. The materials were in the quench aging state and its uniform grain size was around 50 μm. In addition, its compressive yield strength and hardness are 243 MPa. Due to relatively high strength and good plasticity, Al-4.2%Cu alloys were widely used in the aerospace manufacturing field. The main chemical compositions of materials were similar to 2024 aluminum alloys, as shown in Table 1 [5].

Table 1 Chemical compositions of the as-received materials (wt. %)

Fe	Si	Mn	Cu	Mg	Zn	Ti	Al
0.20	0.25	0.30–0.50	3.90–4.50	0.15–0.30	0.10	0.15	Balance

2.2 The schematic of electromagnetic impact and inspection methods

The schematic diagram of electromagnetic impact process and inspection methods were shown in Fig. 1. The electromagnetic impact process mainly included two parts: magnetic pulse generator and impact setup. In this work, the magnetic pulse generator was a 48.8 kJ electromagnetic forming machine (EFM) at the Hunan University [5]. The working principle of the machine could be considered as an energy storage process. The electrical energies were store in capacitor bank by a charging part. The capacitor bank was charged by adjusting the charging parameters and preset electrical energies. When the charging process completed, the store energies were discharged by closing the discharge switch. At the moment, the discharge process could be described as a typical *RLC* oscillation circuit including the system resistance *R*, the flat spiral coil inductance *L* and the capacitance *C*. A changing current with the high amplitude run though the coil during the discharge process. The changing electrical field would lead to a rapidly changing electromagnetic field around it. Meanwhile, an eddy current was induced in diver plate (the copper sheet with high electrical conductivity) which was exposed to the varying magnetic field. And then the other magnetic field was induced by the eddy current. The repulsive forces between the two fields would push the driver plate and punch to impact the specimen. The deformation of EI specimens could be controlled by adjusting the preset discharge energies. To investigate microstructure evolution during the EI process, EI experiments under the varying discharge energies were conducted in this work.

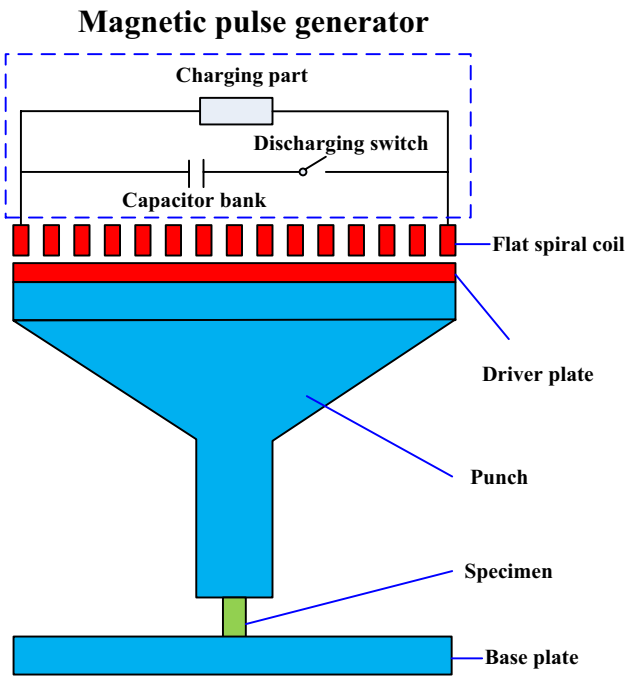

Fig. 1 The schematic diagram of electromagnetic impact process

The deformations of electromagnetic impact specimens generally completed within some milliseconds, leading to a high strain rate and impact velocity. Consequently, the inspection platform was established to reveal deformation behaviors of specimens. A high-speed camera with 20,000 frames per second was used to obtain the impact velocity and loading displacement of the punch.

2.3 Microstructure observation methods

The deformed specimens were cut to use for microstructure observations. The EI specimens were split along its axis and mechanically polished. The OM chemical etchant was a Keller solution of 2.5 ml HNO_3, 1.5 ml HCL, 1 ml HF and 95 ml H_2O. After chemical etching, the corrosion products on the OM (optical microscope) specimens were washed up with a solution of 40% HNO_3 and 60% H_2O. All metallographic observations were performed by an Olympus microscope. After electrolytic polishing with the solution of 200 ml C_2H_5OH and $HClO_4$, SEM (scanning electron microscope) observations were carried out with a Quanta 200FEG scanning electron microscope. To analyze more detailed microstructure evolution, specimens for TEM (transmission electron microscopy) observations were selected on the positions of ASBs. The TEM specimens were mechanically polished to a thickness of 80 μm. After this operations, an etching solution of 30% nitric acid and 70% ethyl alcohol were used to thin them by a twin-jet electro-polishing device. All TEM observations were performed using a TecnaiF2F30 transmission electron microscope.

3 Results and discussion

3.1 Microstructure distribution under impact velocities

The obtained velocity results from high-speed camera are shown in Fig. 2. It could be seen that impact velocity curves had two peaks on the whole. The maximum impact velocities were 4.7 m/s and 6.7 m/s for the discharge energies of 4.0 kJ and 5.0 kJ, respectively. In addition, the deformation resistance and microstructure evolution resulted in the real-time fluctuation of velocities. This also meant that the deformation resistance and work hardening degree were very significant during the electromagnetic impact process. The impact loading completed at 0.9 ms and the braking time of the punch continued until 1.25 ms. The inertia effect drove to the latency process of braking time.

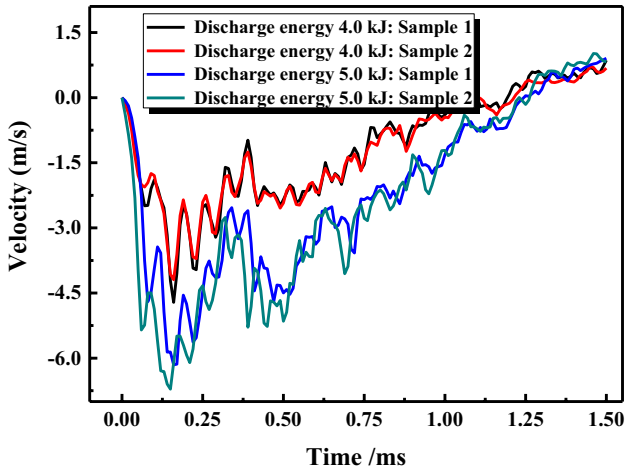

Fig. 2 Impact velocities under varying discharge energies

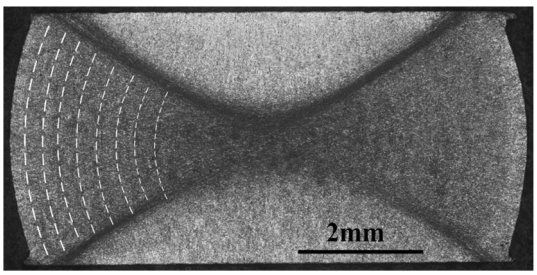

Fig. 3 Microstructure distribution for the discharge energy of 5.0 kJ: two adiabatic shear bands (two parabola-shaped shear deformation areas), the restricted deformation area (upper and lower triangular area) and free deformation area (left and right sector area)

Figure 3 showed the microstructure distribution on the longitudinal section of samples after 5 kJ electromagnetic impact. It could be seen that the deformed sample presented the characteristics of symmetrically drum-like shape. There are two parabola-shaped shear deformation areas in the diagonal of sample. Using the shear deformation microstructures as the boundary, the whole section could be divided into two kind areas: the restricted deformation area (upper and lower triangular area) and free deformation area (left and right sector area). The shear area had so severe deformations that the original equiaxed grain morphology was no longer visible. The grains were completely elongated into fibrous microstructures (known as shear bands). It could be seen in Fig. 2 that the electromagnetic impact ended within 1.25 ms. During the so short deformation process, the heat generated by plastic work was difficult to be lost the surrounding environment. Therefore, the impact process could be considered as adiabatic state and the formed shear bands could be also called as adiabatic shear bands (ASBs). Under the restriction punch and base plate, only grains near the ASBs were plastically deformed in the restricted deformation zone. And the original equiaxed grain morphology was basically retained in other positions. No plastic deformations almost occurred. Microstructures in the free deformation zone could freely flow along the radial direction of cylindrical sample. It could be seen that the microstructures radiated outwards in the form of an arc layer by layer, presenting a streamlined shape. The microstructure deformations were more severe in the positions closer the center. The central position had poor plastic flow and was compressed by the upper and lower restricted deformation areas. Consequently, the position had the most severe deformations.

3.2 The formation mechanism of adiabatic shear bands

According to microstructure distribution characteristic and sample size, some quantitative analysis could be obtained, as shown in Fig. 4. The metals in restricted deformation area had very small plastic deformations due to the friction resistance of punch and base plate. Consequently, this parts could be regarded as a rigid zone and locations of them were only migrated during electromagnetic impact. Because some metals were involved into the adiabatic shear bands, the width

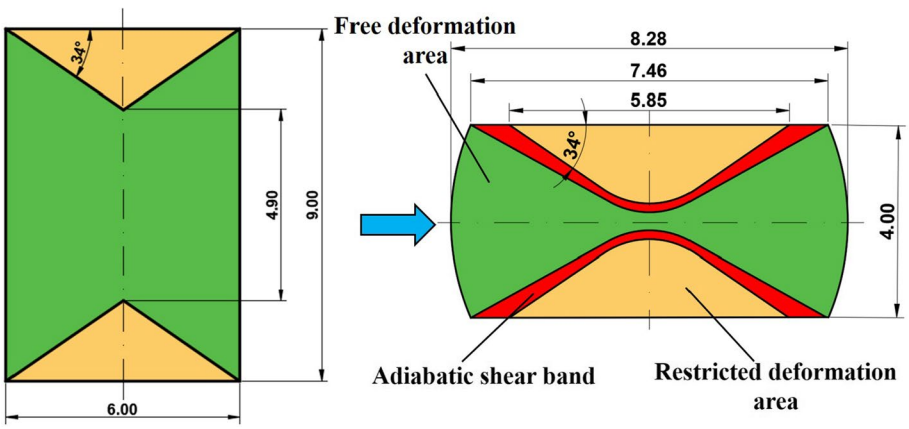

Fig. 4 Microstructure evolution of samples during electromagnetic impact: the deformed picture was equally mapped according to Fig. 3, and microstructures in the restricted deformation area were fully inherited from the original undeformed samples

(values from 6.00 to 5.85 mm) of surfaces contacting tools slightly was decreased. Moreover, the top of the triangle areas was in the three-dimensional compressive stress state. This part was compressed into the arc shape (as shown in Fig. 3).In the free deformation area, the metals were compressed under the upper and lower restricted deformation areas. The free surfaces could simultaneously flow along the radial direction of samples. The midpoint of sample height had shear resistance from restricted deformation areas. The velocity of plastic flow was maximum, causing that the sector areas were formed.

The drum-like shape of free deformation area caused by velocity gradient from the surface layer to inner layer of cylindrical bars. Thus, it could inevitably lead to an increase in shear strain rate and internal deformation work. It could be seen in Fig. 3 that the deformation streamlines were considered as concentric arcs in the free deformation area. The deformation degree decreased layer by layer from inside to outside part of samples. The shape of the deformed sample was axisymmetric. Consequently, the plane deformation model could be selected with the Cartesian coordinate system in this paper. Figure 5 showed evolution model in varying deformation areas during electromagnetic impact. Consequently, it could be considered that velocity component v_x (along x coordinate axis) changed in the form of a linear function along x coordinate axis. The velocity component varied in the form of arc curve along y coordinate axis. According to the size data in Fig. 4, the arc curve could be simplified as an exponential function. Consequently, the velocity component could be assumed as Eq. (1), where a and b were undetermined coefficients. The parameters v and h were the impact velocity and the height (9 mm) of original samples, respectively.

$$v_x = av\frac{2x}{h}e^{-2by/h} \tag{1}$$

The volume of sample remained a constant during the deformation process, so strain rates could be obtained by:

$$\dot{\varepsilon}_z = 0$$
$$\dot{\varepsilon}_x = \frac{\partial v_x}{\partial x} = \frac{2av}{h}e^{-2by/h} = -\dot{\varepsilon}_y = \frac{\partial v_y}{\partial y} \tag{2}$$

Integrating the Eq. (2), the velocity component v_y (along y coordinate axis) could be obtained.

$$v_y = -\frac{2av}{h}\int e^{-2by/h}dy = \frac{a}{b}v\int e^{-2by/h} + f(x) \tag{3}$$

Due to the symmetry of deformed sample, v_y was zero when the y coordinate equaled to zero. Substituting this condition to Eq. (3), the velocity component v_y could be described as:

$$v_y = \frac{a}{b}v\left(e^{-2by/h} - 1\right) \tag{4}$$

The velocity at positions contacting to the rigid restricted deformation area was v. the $v_y = -v$ when the y coordinate was $h/2$. So,

$$v_y\Big|_{y=h/2} = \frac{a}{b}v(e^{-b} - 1) = v$$

$$a = \frac{b}{e^{-b} - 1}$$

According to measured data of arc curve, the fitting curve could be obtained using an exponential function, as depicted in Fig. 6. It could be seen that the fitting curve agreed well with the measured results. Consequently, the undetermined coefficients a and b were calculated as 0.66 and 0.77, respectively. The velocity component v_x could also be obtained during the electromagnetic loading, as shown in Fig. 7. It could be seen that the velocity was increased from inner to outside part of samples. And it was also increased from two sides to middle position of the height of sample.

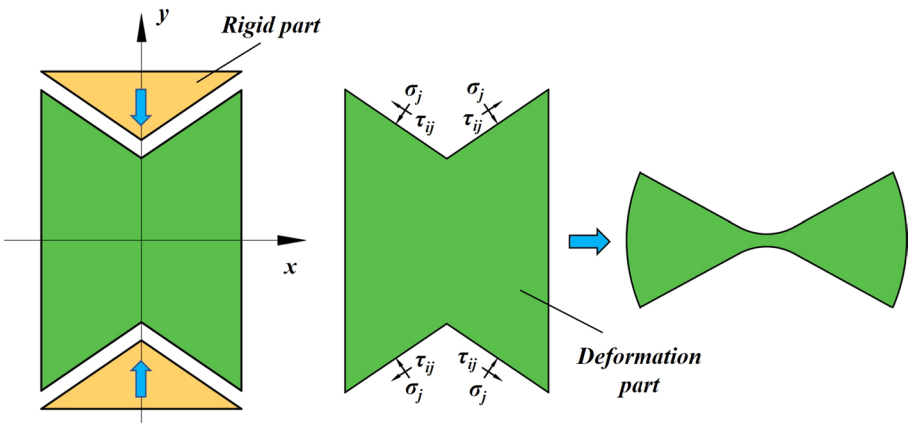

Fig. 5 Evolution model in varying deformation areas during electromagnetic impact: the upper and lower restricted deformation areas was considered as rigid parts; the rigid parts impacted and compressed the central part into sectors

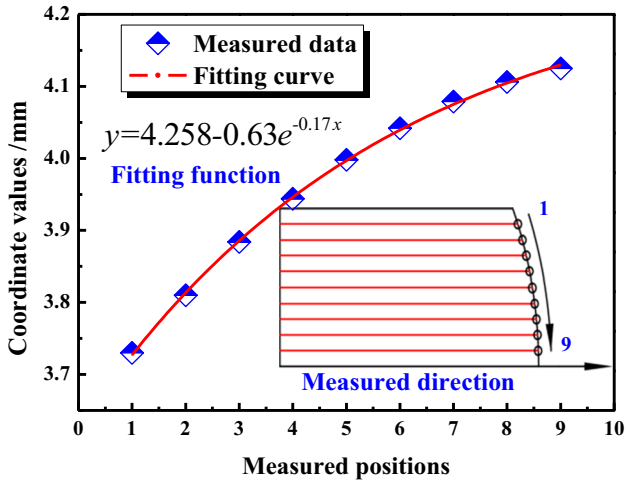

Fig. 6 The fitting of arc curve using an exponential function: the side profile of deformed samples accorded with exponential function ($y = 4.258–0.63e^{-0.17x}$)

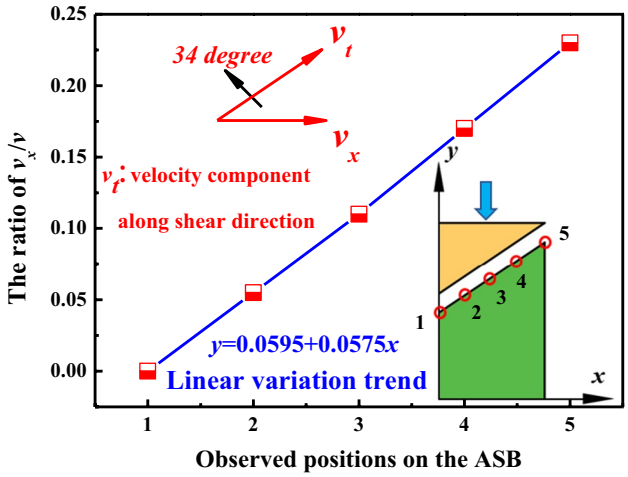

Fig. 8 The velocity component v_x/v on the adiabatic shear band: velocity component (v_t) along shear direction equaled $v_x$cos34°; the velocity (v_t) accorded with linear distribution law

This distribution law directly caused the drum-like shape of deformed sample. Previous tests on impact velocity showed the maximum value reached up to 6.7 m/s, giving rise to a velocity component v_x of 3.0 m/s. This velocity was very great relative to so small radius (3 mm) of sample and short loading time (1.25 ms).

The velocity component v_x on the adiabatic shear band was shown in Fig. 8. It could be seen that the velocity component v_x had a linear variation trend. And the velocity gradually increased from inner to outside samples. The included angle was 34° between the direction of velocity component v_x and shear direction. Consequently, the velocity component v_t along the shear direction could be calculated with $v_x$cos34° and had identical changing law with that of velocity component v_x. Due to the materials continuity rule, the velocity component v_y along y coordinate axis was same at contact locations between restricted deformation area and free deformation area. The metals at the contact locations simultaneously moved downward under the effect of velocity component v_y, which did not cause shear deformations. However, the metals in the restricted deformation area had very small plastic deformations, resulting in almost no plastic flow along the x coordinate axis. The velocity component v_x and v_t were basically zero in the restricted deformation area. Thus, the velocity gradient inevitably caused shear deformations at contact locations between the restricted deformation area and free deformation area. Moreover, the velocity gradient values gradually decreased from outside to inner part of samples. The shear deformations initiated at diagonal points and gradually expanded into the center of original samples, and encountered around the central position. Figure 9 showed that microstructure distributions for the discharge energies of 3.0 kJ and 4.0 kJ. Previous analysis presented that samples with high discharge energies had great plastic deformations. Therefore, adiabatic shear

Fig. 7 The calculated results of velocity component v_x/v: the 1/4 calculated part was selected due to axial symmetry structure

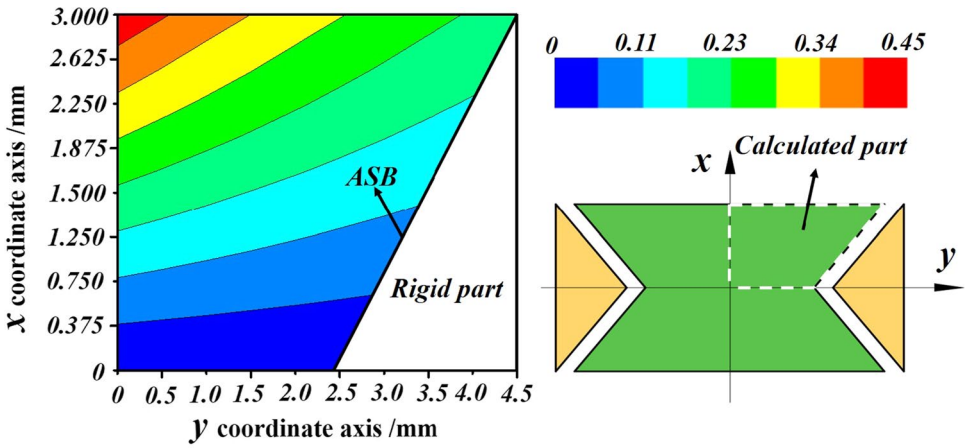

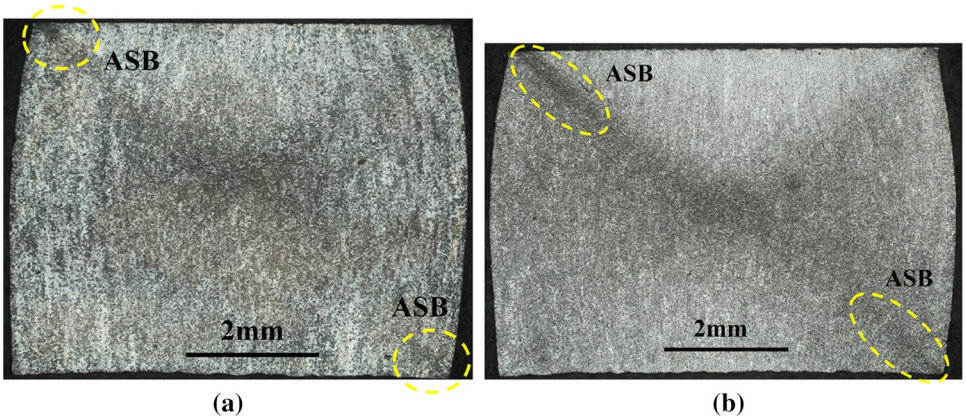

Fig. 9 Microstructure distributions for varying discharge energies: **a** microstructures of the ASB initiation stage under the discharge of 3.0 kJ; **b** microstructures of the ASB propagation stage under the discharge of 4.0 kJ

bands started at diagonal points of samples under the discharge energy of 3.0 kJ. And the ASBs gradually extended into the center of samples as deformations increased. This microstructure evolution trend corresponded with that of shearing velocity gradient.

3.3 Microstructure evolution in adiabatic shear bands

SEM microstructure morphologies in different deformation areas were shown in Fig. 10. It could be seen that microstructures in restricted deformation area still kept equiaxial grain morphology. In the free deformation area, grains were elongated along the radial direction of drum-like

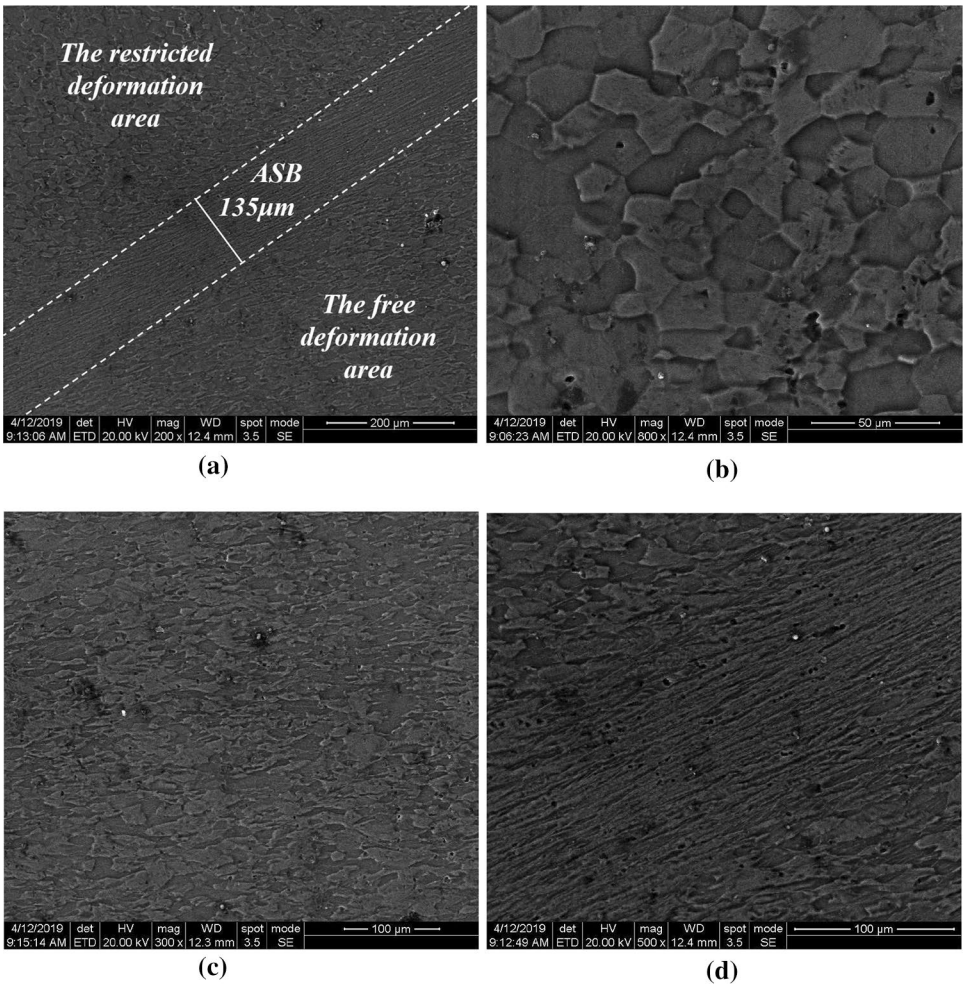

Fig. 10 SEM microstructure morphologies in the different deformation areas: **a** whole microstructure morphologies, **b** restricted deformation area, **c** free deformation area, **d** adiabatic shear band

sample. Some grains were distorted and refined into subgrains. The laminated microstructures were formed inside adiabatic shear bands, and the width of ASBs was about 135 μm. Consequently, the deformation process within the ASBs could be approximately considered as a pure shear deformation, as shown in Fig. 11. The ASBs were formed by the relative movement between the quiescent restricted deformation area and radial flowing free deformation area. The plastic flow velocity v_t along the shear direction could be calculated in the Fig. 8. The shear deformation values γ could be demonstrated the following Eq. (5), where the line AB in Fig. 11 was presented as the width (135 μm) of ASBs. For pure shear deformation, the effective strain ε_f could be described as Eq. (7).

$$\tan\gamma = \frac{BC}{AB} \tag{5}$$

$$BC = v_t t = v_x t \cos 34^\circ \tag{6}$$

$$\varepsilon_f = \frac{1}{\sqrt{3}}\gamma \tag{7}$$

The whole deformation process completed within 1.25 ms, causing that plastic deformation heat could not be quickly lost in the surrounding. The plastic deformation heat was converted by the plastic work. Consequently, the adiabatic temperature rise ΔT could be approximately calculated with the following Eq. (8).

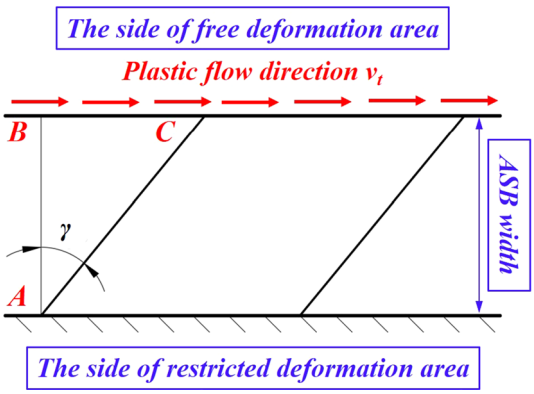

Fig. 11 The deformation model within adiabatic shear band: the side of restricted deformation area was seen as rigid part and was equivalent to being stationary, the plastic flow velocity component (v_t) existed in the side of free deformation area; the shear deformations within ASBs were regarded as pure shear process and ASB width could be measured in Fig. 10a

$$\Delta T = \frac{\beta}{\rho c}\int_0^{\varepsilon_f} \sigma \mathrm{d}\varepsilon \tag{8}$$

where β is the coefficient (0.9 in general) of heat conversion, ε_f is the final effective strain. ρ is material density (2660 kg/m^3 for aluminum alloy), and σ is the stress (MPa). The specific heat capacity c of aluminum alloy are 2660 kg/m^3 and 880 J/(kg °C). The stress–strain relationship under high-speed impact could be characterized using the Johnson–Cook constitutive model (Eq. (9)) [26].

$$\sigma = (A + B\varepsilon^n)\left(1 + C\ln\frac{\dot{\varepsilon}}{\dot{\varepsilon}_0}\right)\left[1 - (T^*)^m\right] \tag{9}$$

$$T^* = \frac{T - T_{\mathrm{room}}}{T_{\mathrm{m}} - T_{\mathrm{room}}} \tag{10}$$

where ε is plastic strain, $\dot{\varepsilon}$ is strain rate (/s) and $\dot{\varepsilon}_0$ is 0.01/s (the reference strain rate). A is yield strength (MPa). B is the hardening coefficient (MPa), C is the strain rate, n is the sensitivity coefficient of hardening coefficient and m is the coefficient of thermal softening. T is the temperature during impact deformations (°C), T_{m} is the melting point of materials (660 ℃) and T_{room} is surrounding temperature (20 ℃). These parameters (A, B, C, m and n) for 2A10 aluminum alloys obtained by Zhang et al. [27] are 243.0, 618.8, 0.01, 1.6 and 0.2, respectively.

By substituting Eqs. (9) to (8), the following equation [28] can be obtained:

$$\int_{T_0^*}^{T^*} \frac{\mathrm{d}T^*}{1 - (T^*)^m} = \frac{0.9\left(1 + C\ln\frac{\dot{\varepsilon}}{\dot{\varepsilon}_0}\right)}{\rho c}\int_0^{\varepsilon_f} (A + B\varepsilon^n)\mathrm{d}\varepsilon \tag{11}$$

The parameter m was in between integer 1 and 2, the Eq. (11) could be simplified by extremum method. $m=1$ and $m=2$ corresponded to the upper and lower boundaries of temperature rise, respectively. Consequently, the integral Eq. (11) could be simplified as:

For the upper boundary $m=1$,

$$T = 20 + 640\left[1 - \exp\left(-0.14\varepsilon_f - 0.31\varepsilon_f^{1.2}\right)\right] \tag{12}$$

For the lower boundary $m=2$,

$$T = 660 - \frac{1280}{1 + \exp\left(0.33\varepsilon_f + 0.69\varepsilon_f^{1.2}\right)} \tag{13}$$

By solving Eqs. (12) and (13), the relationship of temperature rise (T) and effective strain (ε_f) was obtained, as shown in Fig. 12a. According to the radial velocity distribution law in Fig. 7, the maximum radial velocity v_x was 045 times bigger that the impact velocity (as shown in Fig. 2b). Using the Eqs. (5)–(7), the effective strain of ASBs could be obtained, as depicted in Fig. 12b. The final effective strain was about

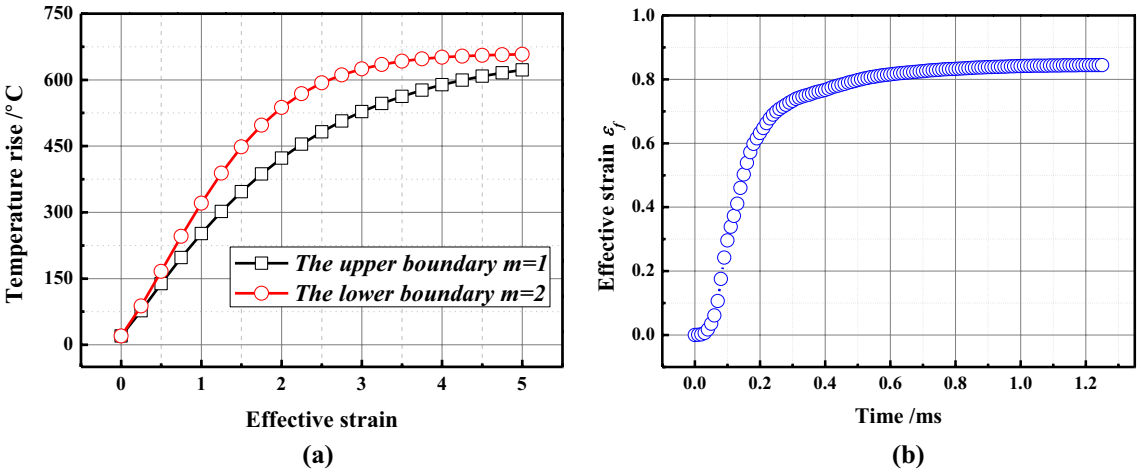

Fig. 12 The temperature rise and effective strain within adiabatic shear band: **a** the relationship between temperature rise and effective strain was for the upper and lower boundaries; **b** shear effective strain–time changing curve

0.845 after the electromagnetic impact deformation. Consequently, it could be calculated that temperature rise was around 218–275 °C (0.33–0.42T_m) within ASBs. The thermal softening effect (rooted from temperature rise) could also facilitate shear deformations inside ASBs. This mutual promoted effect between shear deformations and thermal softening would aggravate the deformation localization, and then resulting in the formation of adiabatic shear bands.

Through the TEM microstructure observations, microstructure evolution within the ASBs could be obtained, as shown in Fig. 13. SEM microstructure observations within ASBs showed laminated morphologies. It could be seen that some laminated microstructures (Fig. 13b) distributed along the same direction. The most laminated microstructures (Fig. 13a) intersected with each other. The included angle was about 60° between the cross laminates. The included angle of slip planes was just 60° for face-centered cubic alloys (Al-4.2%Cu aluminum alloys in this work). This indicated that multi-slip systems were simultaneously actuated due to severe shear deformations. The cross slips occurred among slip planes with different directions. In addition, the width of laminated microstructures was non-uniform. The minimum and maximum widths were about 1 μm and 2.3 μm, respectively. The laminated microstructures included high-density dislocations (Fig. 13c) due to significant shear deformations inside ASBs. The increase in dislocation density was responsible for serious dislocation tangles. Consequently, dislocation pattern was mainly reflected by dislocation tangles (Fig. 13d). The distortion energies increased significantly and were stored in adiabatic shear bands.

Remarkable distortion energies could provide further evolution of microstructures with driving forces. Many equiaxial grains were found in the ASBs, as shown in Fig. 14. The size of these grains was inhomogeneous and was about 70–280 nm. The electromagnetic impact deformation was completed within 1.25 ms, and the maximum temperature rise reached up to 275 °C during short process. After this, the temperature rise quickly dispersed and restored to room temperature due to no temperature prevention. Therefore, the formation mechanism of equiaxial grains was different from the conventional recrystallization (temperature rise and holding time). Meyers et al. [20, 21] proposed a rotational dynamic recrystallization model (Fig. 15) for adiabatic shearing processes. At the initial shearing deformation, high-density dislocations uniformly distributed in the deformed grains. With the continuous deformation, the cumulative misorientation also dramatically increased to associate with dislocation arrangement. High-density dislocations were saturated interacted and tangled with each other, resulting in the formation of sub-grains. Original equiaxial grains were elongated into strip sub-grains along the shearing direction. The strip sub-grains were further sheared and refined, and refined sub-grains still distributed along shearing direction. Finally, sub-grains were rotated under the driving effect of adiabatic temperature rise and distortion energies. Sub-grains were rotated by 30°, causing that small angle grain-boundaries could be transformed into large angle grain-boundaries. So the rotated sub-grains were evolved into observed recrystallization grains.

The rotational recrystallization mechanism was established from the perspective of dislocation movements. Kinetic equations for sub-grain rotations were described as:

$$t = \frac{L_1 Tkf(\theta)}{4\delta\eta D_{b0}\exp(-Q_b/RT)} \tag{14}$$

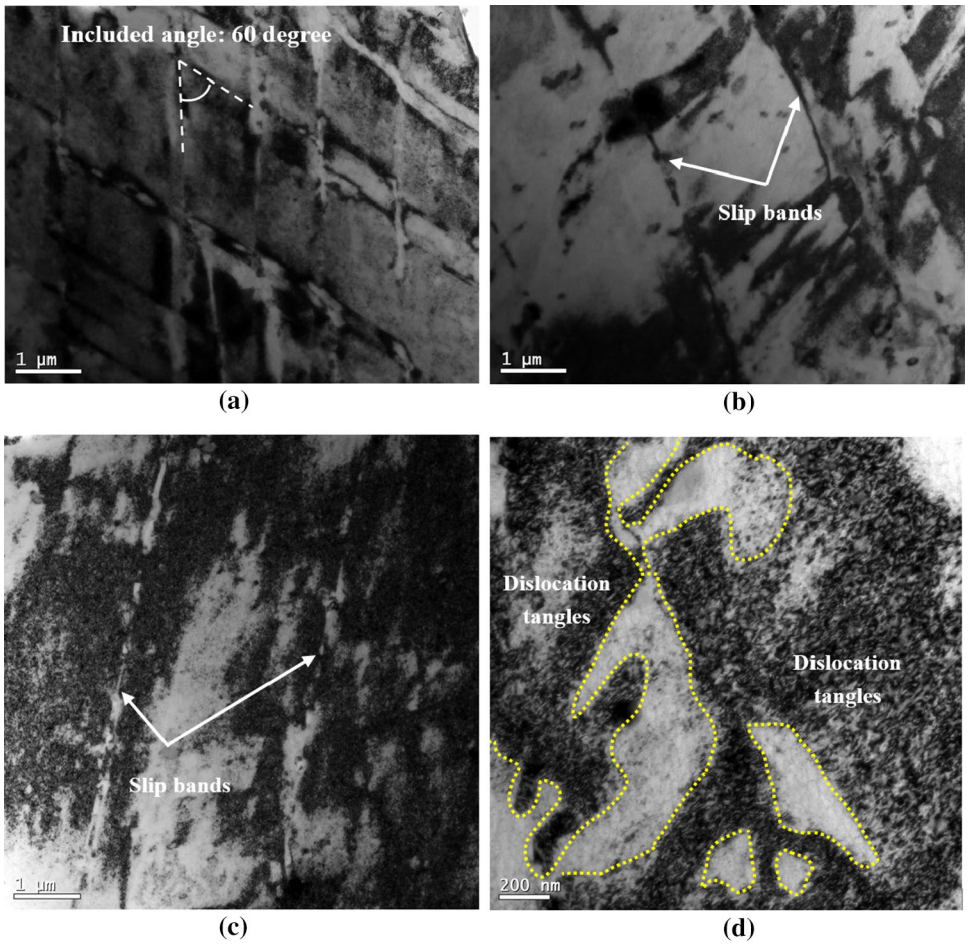

Fig. 13 TEM microstructure morphologies within the adiabatic shear bands: **a** the included angel was 60° for two cross slips(two slip systems for face-center cubic materials); **b** unidirectional shear slip band; **c** unidirectional shear slip band and dislocation pattern; **d** dislocation tangles among the high-density dislocations

$$f(\theta) = \frac{3\tan(\theta) - 2\cos(\theta)}{3 - 6\sin(\theta)} + \frac{2}{3} - \frac{4\sqrt{3}}{9}\ln\frac{2+\sqrt{3}}{2-\sqrt{3}} + \frac{4\sqrt{3}}{9}\ln\frac{\tan(\theta/2) - 2 - \sqrt{3}}{\tan(\theta/2) - 2 + \sqrt{3}} \quad (15)$$

where t was the needed time for the formation of recrystallization grains, T was heating temperature, L_1 was equiaxial grain size, θ was misorientation of sub-grains, η was grain boundary energy, δ was grain-boundary thickness, D_{b0} was the grain-boundary diffusion coefficient, Q_b was activation energy for grain boundary diffusion and was 0.4–0.6 times greater than activation energy (Q) for grain growth. R was molar gas constant (8.314 J/mol K) and k was Boltzmann's constant (1.38×10^{-23} J/K).

For aluminum alloys, grain boundary energy η was 0.35 J/m^2 and activation energy Q_b was 86.4 kJ/mol (0.6 Q) [29]. The δD_{b0} was 9.9×10^{-14} m^3/s for aluminum alloys [25]. Adiabatic temperature rise (0.33–0.42 T_m) and recrystallization grain size (70–280 nm) were calculated in previous analysis. Substituting these parameters into Eqs. (14) and (15), the relationship between the rotated angle and recrystallization time could be obtained, as demonstrated in Fig. 16. It could be seen in Fig. 16a that generating recrystallization grains with the size of 175 nm (average size) needed much shorter time under higher adiabatic temperature rise. Figure 16b showed that smaller recrystallization grains were generated much sooner. The maximum time completing rotational recrystallization was about 45 μs, which was far less than lasting time of the whole electromagnetic impact deformation. Consequently, sub-grains had sufficient rotation time to form recrystallization grain.

4 Conclusion

This paper mainly investigated the formation of adiabatic shear bands and microstructure evolution of Al-4.2%Cu alloy bar by electromagnetic loading. The theoretical model was proposed to reveal the formation of ASBs and obtain adiabatic temperature rise. The SEM and TEM microstructure observations were employed to characterize microstructure evolution inside ASBs. The conclusions drawn from the results could be summarized as follows:

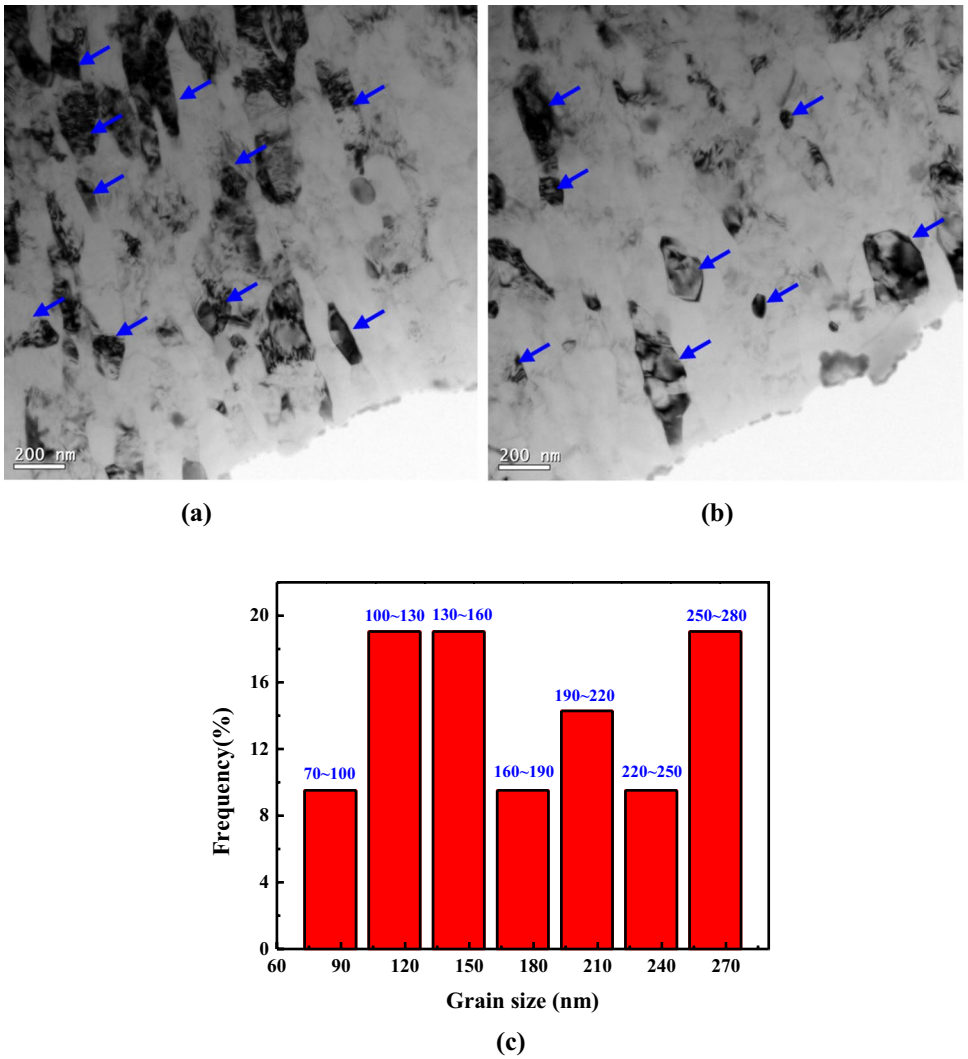

Fig. 14 Dynamic recrystallization grains (blue arrows) within the adiabatic shear bands: **a** equiaxial grain morphologies in observed position 1, **b** equiaxial grain morphologies in observed position 2, **c** statistics data of grain size of observed equiaxial grains in Fig. 14a and b

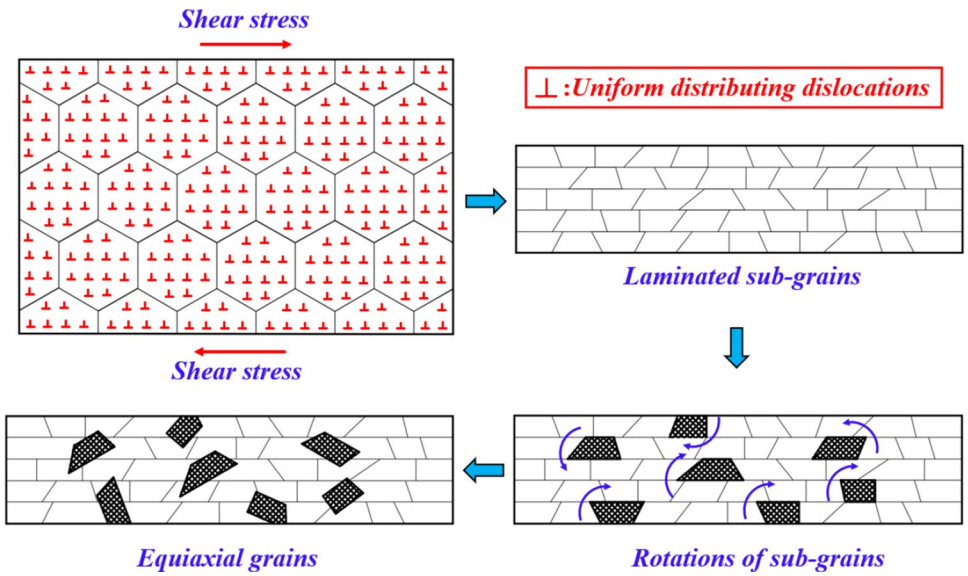

Fig. 15 Dynamic recrystallization model by rotations of sub-grains: dislocations in grains presented uniform distribution during initial stage of shear deformations; the original grains with equiaxial shape were elongated into laminated sub-grains; the distorted sub-grains were rotated; the equiaxial dynamic recrystallization grains were generated

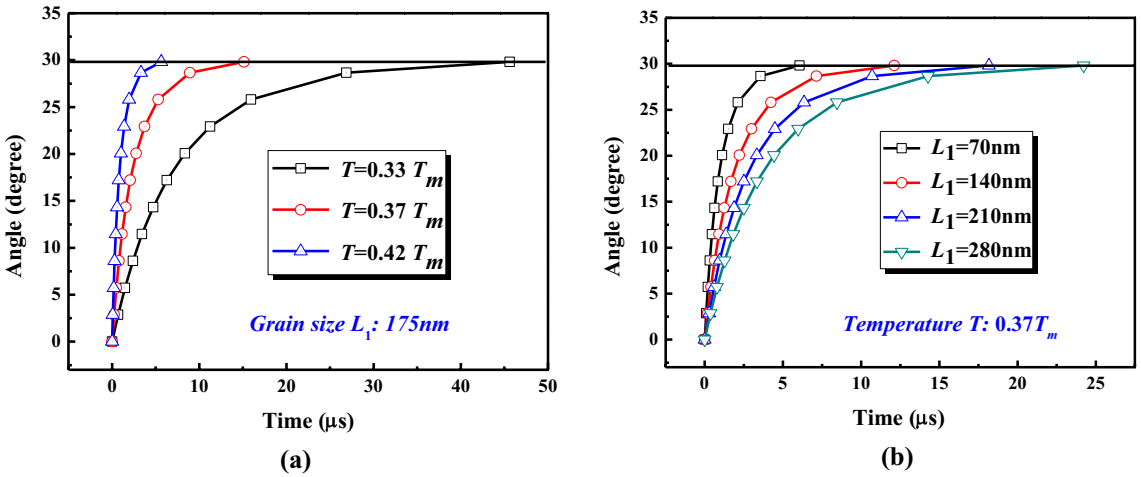

Fig. 16 The relationship of the rotated angle and recrystallization time: **a** at different temperature and same grain size (grain size L_1: 175 nm is the mean of measured values), **b** at different grain size and same temperature (temperature T: 0.37 T_m is the mean of calculated values)

1. The peak values of impact velocity reached up to 6.7 m/s during the electromagnetic loading process, respectively. This gave rise to a high strain rate and loading stress within a short deformation time (1.25 ms).
2. The theoretical model indicated that the radial velocity gradient contributed to the formation of ASBs. The velocity gradient was generated between the rigid restricted deformation area and free deformation area. In addition, the shearing velocity component (v_t) decreased from diagonal points to center of samples, showing that the ASBs gradually extended into the center of samples as deformations increased.
3. The severe deformations were concentrated within the adiabatic shear bands. Pure shear deformations resulted in adiabatic temperature rise of 0.33–0.42 T_m inside ASBs. The width of ASBs was about 135 μm, where original equiaxial grains were significantly elongated into laminated sub-structures.
4. TEM microstructures demonstrated multi-slip systems (included angle 60°) were simultaneously actuated inside ASBs because of severe pure shear deformations. Adiabatic temperature rise and distorted energies from dislocation tangles drove sub-grains rotate into recrystallization grains (70–280 nm).
5. The needed maximum time (45 μs) for rotational dynamic recrystallization was far less than that of electromagnetic impact deformation, implying that rotational dynamic recrystallization mechanism contributed to the formation of recrystallization grains.

Funding This work was supported by the Natural Science Foundation of Hunan Province (Grant no. 2019JJ50662), Education Department of Hunan Province (Grant no. 18C0208) and National Key Research and Development Program of Hunan Province (Grant no. 2017GK2090).

References

1. Zhang XX, Zhou XR, Hashimoto T, Liu B, Luo C, Sun ZH, Tang ZH, Lu F, Ma YL. Corrosion behaviour of 2A97-T6 Al-Cu-Li alloy: the influence of non-uniform precipitation. Corros Sci. 2018;132:1–8.
2. Nie HL, Suo T, Wu BB, Li YL, Zhao H. A versatile split Hopkinson pressure bar using electromagnetic loading. Int J Impact Eng. 2018;116:94–104.
3. González EV, Maimí P, Camanho PP, Turon A, Mayugo JA. Simulation of drop-weight impact and compression after impact tests on composite laminates. Compos Struct. 2012;94:3364–78.
4. Psyk V, Risch D, Kinsey BL, Tekkaya AE, Kleiner M. Electromagnetic forming—a review. J Mater Process Technol. 2011;211:787–829.
5. Zhang X, Cui JJ, Xu JR, Li GY. Microstructure investigations on 2A10 aluminum alloy bars subjected to electromagnetic impact upsetting. Mater Sci Eng A. 2017;702:142–50.
6. Zhang X, Cui JJ, Li GY. Microstructural mechanism in adiabatic shear bands of Al-Cu alloy bars using electromagnetic impact upsetting. Mater Lett. 2017;194:62–5.
7. Wright TW. The physics and mathematics of adiabatic shear bands. Cambridge: Cambridge University Press; 2002.
8. Tresca MH. On further applications of the flow of solids. J Frankl Inst. 1878;106:326–34.
9. Zener C, Hollomon JH. Effect of strain rate upon plastic flow of steel. J Appl Phys. 1944;15:22–3.
10. Bai YL. Thermo-plastic instability in simple shear. J Mech Phys Solids. 1982;30:195–207.
11. Ranc N, Taravella L, Pina V, Herve P. Mech Mater. 2008;40:255–70.
12. Li ZZ, Wang BF, Zhao ST, Valiev RZ, Vecchio KS, Meyers MA. Dynamic deformation and failure of ultrafine-grained titanium. Acta Mater. 2017;125:210–8.
13. Li JG, Li YL, Huang CX, Suo T, Wei QM. On adiabatic shear localization in nanostructured face-centered cubic alloys with different stacking fault energies. Acta Mater. 2017;141:163–82.
14. McAuliffe C, Waisman H. A unified model for metal failure capturing shear banding and fracture. Int J Plasticity. 2015;65:131–51.
15. Bejjani R, Balazinski M, Attia H, Plamondon P, L'Espérance G. Chip formation and microstructure evolution in the adiabatic shear

band when machining titanium metal matrix composites. Int J Mach Tool Manu. 2016;109:137–46.
16. Yang Y, Jiang F, Zhou BM, Li XM, Zheng HG, Zhang QM. Microstructural characterization and evolution mechanism of adiabatic shear band in a near beta-Ti alloy. Mater Sci Eng A. 2011;528:2787–94.
17. Kad BK, Gebert JM, Perez-Prado MT, Kassner ME, Meyers MA. Ultrafine-grain-sized zirconium by dynamic deformation. Acta Mater. 2006;54:4111–27.
18. Peirs J, Tirry W, Amin-Ahmadi B, Coghe F, Verleysen P, Rabet L, Schryvers D, Degrieck J. Microstructure of adiabatic shear bands in Ti6Al4V. Mater Charact. 2013;75:79–92.
19. Hines JA, Vecchio KS, Ahzi SA. A model for microstructure evolution in adiabatic shear bands. Met And Mat Trans A. 1998;29:191–203.
20. Meyers MA, Xu YB, Xue Q. Microstructural evolution in adiabatic shear localization in stainless steel. Acta Mater. 2003;51:1307–25.
21. Nesterenko VF, Meyers MA, Lasalvia JC. Shear localization and recrystallization in high-strain, high-strain-rate deformation of tantalum. Mater Sci Eng A. 1997;229:23–41.
22. Boakye-Yiadom S, Bassim N. Microstructural evolution of adiabatic shear bands in pure copper during impact at high strain rates. Mater Sci Eng A. 2018;711:182–94.
23. Yang Y, Wang BF. Dynamic recrystallization in adiabatic shear band in α-titanium. Mater Lett. 2006;60:2198–202.
24. Zhang X, Zhu CC, Hu L, Wu HQ, Li CF. Investigations on microstructure evolution of TA1 titanium alloy subjected to electromagnetic impact loading. Arch Civ Mech Eng. 2019;19:639–47.
25. Wang BF, Ma R, Zhou JD, Li ZZ, Zhao ST, Huang XX. Adiabatic shear localization in ultrafine grained 6061 aluminum alloy. Mater Sci Eng A. 2016;675:221–7.
26. Johnson RG, Cook WH. A constitutive model and data for metals subjected to large strain, high strain rates and high temperatures. In: Proceedings of the 7th international symposium on ballistics; 1983. pp. 541–547.
27. Zhang X, Yu HP, Li CF. Multi-filed coupling numerical simulation and experimental investigation in electromagnetic riveting. Int J Adv Manuf Technol. 2014;73:1751–63.
28. Zhang X, Yu HP, Li J, Li CF. Microstructure investigation and mechanical property analysis in electromagnetic riveting. Int J Adv Manuf Technol. 2015;78:613–23.
29. Smallman RE. Modern physical metallurgy. Amsterdam: Elsevier; 1962.

Publisher's Note Springer Nature remains neutral with regard to jurisdictional claims in published maps and institutional affiliations.